Supplement of Atmos. Chem. Phys., 26, 4509–4529, 2026
https://doi.org/10.5194/acp-26-4509-2026-supplement

Supplement of

Inferring drivers of tropical isoprene: competing effects of emissions and chemistry

James Young Suk Yoon et al.

Correspondence to: Alexander J. Turner (turneraj@uw.edu)

Supplement

Introduction

This supplement contains 21 total additional figures.

Section 1 contains supplemental figures relating to thermal infrared radiative transfer modeling. This includes isoprene absorption cross sections (Fig. S1); the MERRA-2 temperature and specific humidity profiles used as input for the model (Fig. S2); the instrument kernel (Fig. S3); and a replication of Figure 6 in the manuscript but with convolved radiance output rather than the differences between spectra (Fig. S4).

Section 2 contains supplemental figures relating to the CrIS retrievals and isoprene regressions. Figure S5 is a time series of non-cloudy scenes in the tropics for the CrIS retrieval, and Figure S6 shows correlations between isoprene mean anomalies and the number of datapoints within each CrIS 0.5° x 0.625° gridbox. Figure S7 reproduces Figure 2 in the manuscript but with vapor pressure deficit (VPD) instead of surface air temperature, and diffuse PAR instead of direct PAR. Figure S8 shows the anti-correlation between leaf area index (LAI) anomalies and isoprene column anomalies over the Maritime Continent. Figure S9 duplicates Figure 7 in the manuscript but with the non-anomalized GFED4 dry matter and MERRA-2 surface air temperatures rather than their anomalies. Figure S10-11 show the seasonal cycles of isoprene columns, isoprene emissions, soil $\mathrm{NO_x}$, and biomass burning in the three regions of interest. Figure S12 shows correlations between non-anomalized isoprene columns and biomass-burning/soil $\mathrm{NO_x}$. Figures S13–S15 show the spatial heterogeneity of isoprene and $\mathrm{NO_x}$ sources, as well as the averaged wind vectors over different seasons. Figure S16 shows the distribution of oil palm plantations across the tropics relative to isoprene column retrievals.

Section 3 contains supplemental figures pertaining to the GEOS-Chem $\mathrm{NO_x}$ **sensitivity studies.** Figure S17 shows the total $\mathrm{NO_x}$ flux changes in the perturbation runs. Figures S18-19 show how isoprene and formaldehyde are affected by the decrease in $\mathrm{NO_x}$. Figure S20 plots the ISOP:HCHO ratio taken from CrIS and OMI observations as a supplement to Figure 9 in the manuscript. Finally, Figure S21 shows column-averaged $J_{O(^1D)}$ and J_{NO_2} simulated in GEOS-Chem across the three tropical regions.

1 Radiative Transfer Modeling

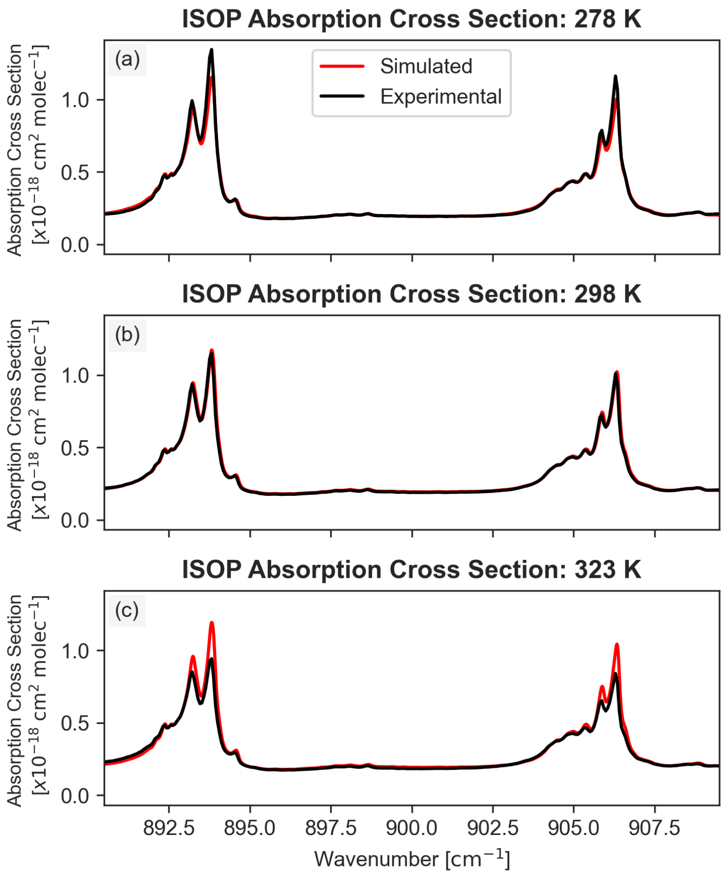

Figure S1: **Isoprene absorption cross sections.** (a) Isoprene absorption cross sections (red) calculated using vSmartMOM's Absorption module for 278 K and 1 atm. Experimental spectra (black) are from Brauer et al. (2014), which took measurements at 0.112 cm^{-1} spectral resolution. Corresponding absorption cross sections for 298 K and 323 K are shown in (b) and (c), respectively.

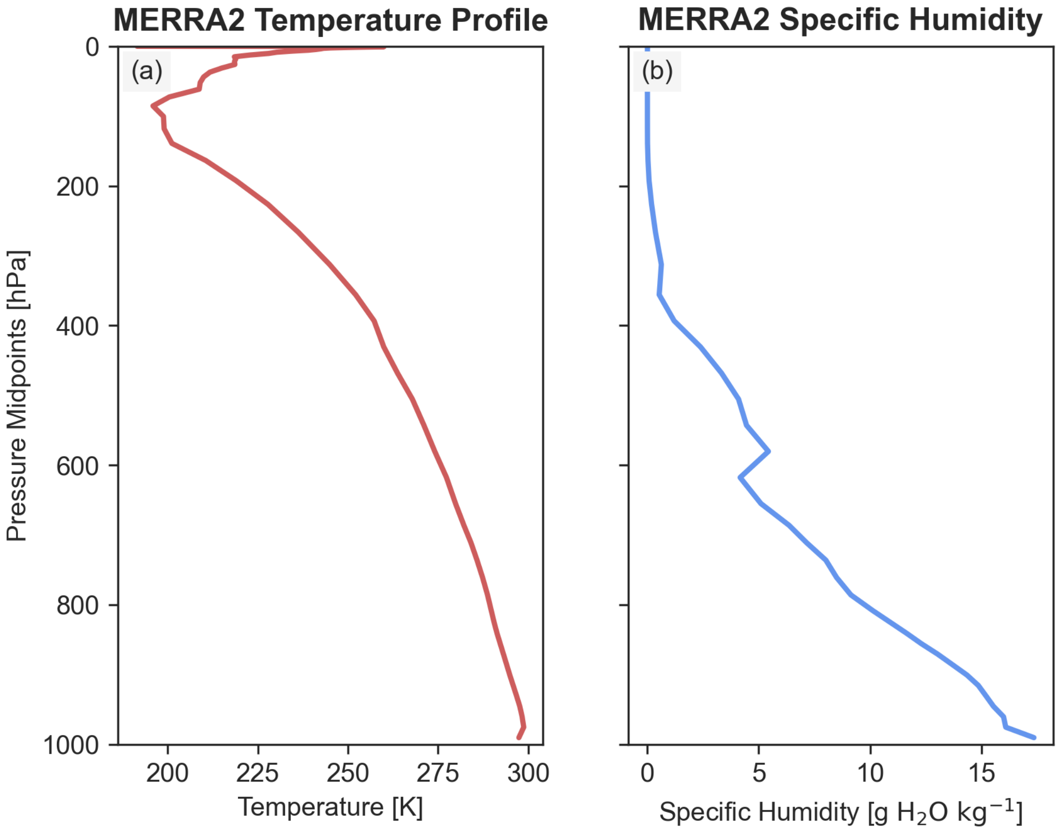

Figure S2: **MERRA-2 profiles.** MERRA2 temperature (a) and specific humidity (b) profiles used in the radiative transfer simulations, characteristic of Sumatra on July 1st, 2019 at 6Z (1 PM local time).

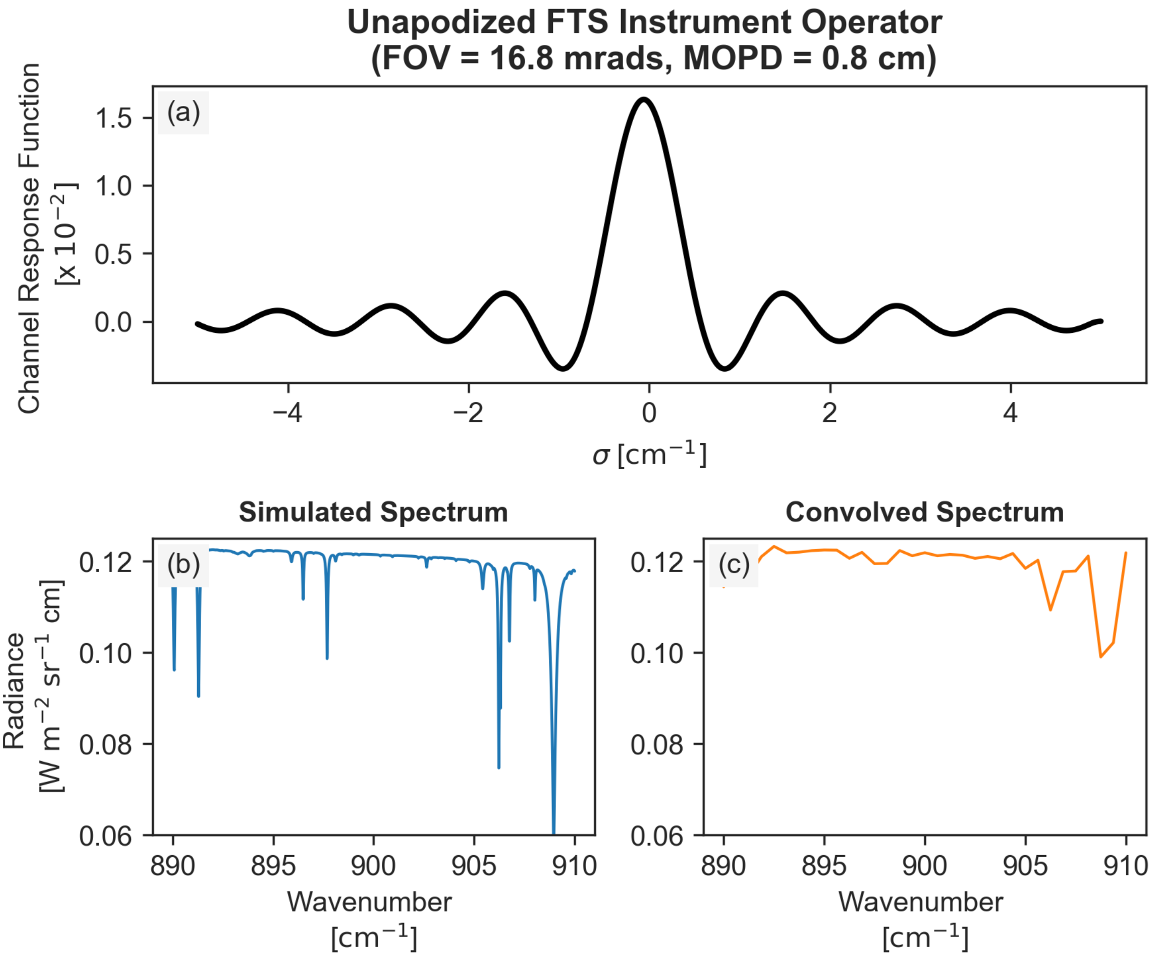

Figure S3: **Instrument kernel.** (a) The unapodized Fourier-transform spectrometer instrument kernel used to convolve the simulated spectra, generated using a field-of-view of 16.8 mrads and a maximum optical path difference of 0.8 cm. (b) A sample simulated spectrum with CO_2, O_2, H_2O, and ISOP (x5 profile), generated using 0.01 cm^{-1} spectral resolution. (c) The corresponding convolved spectra with 0.625 cm^{-1} spectral resolution.

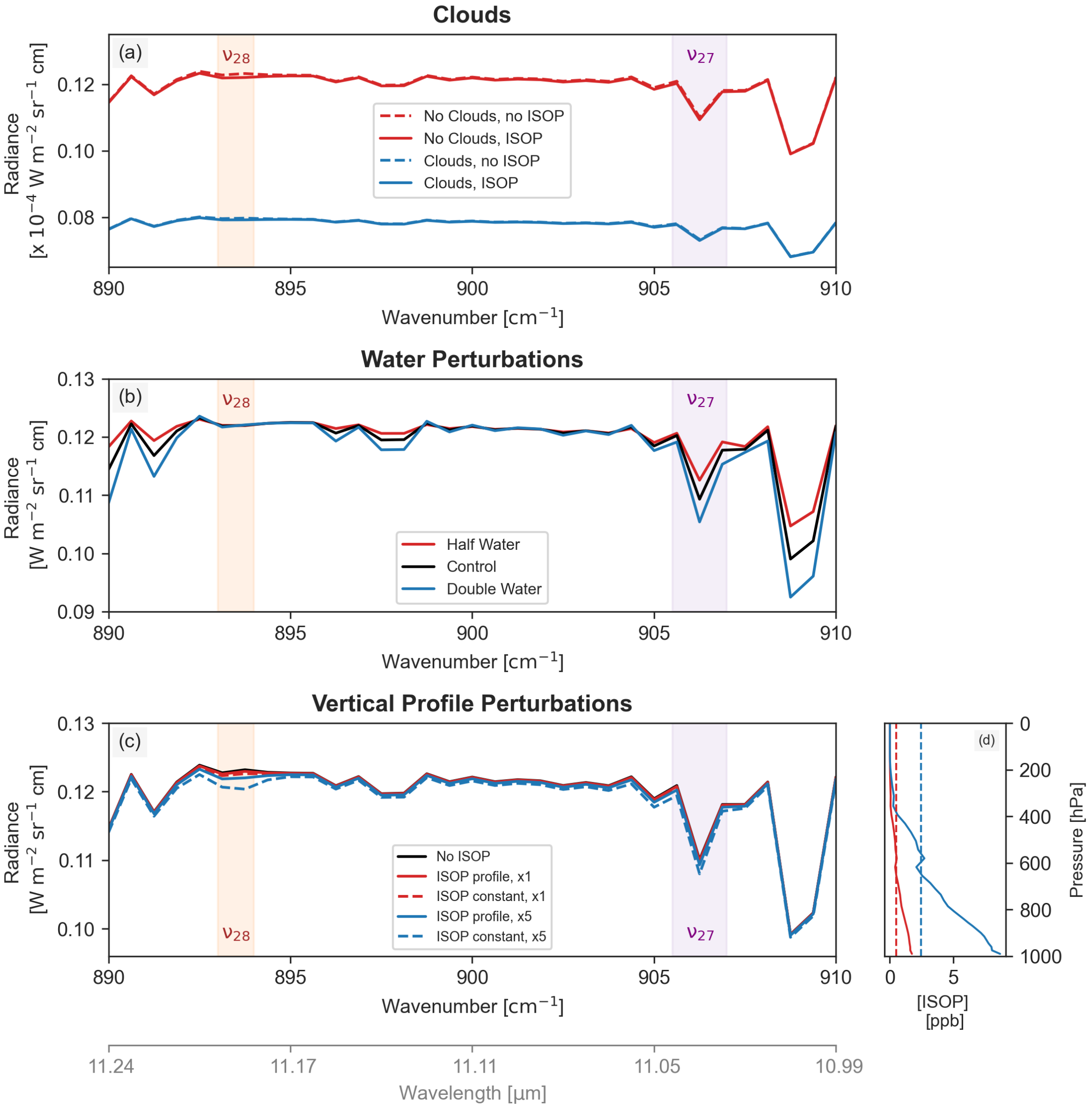

Figure S4: **Raw convolved radiances.** Figure 6 in the manuscript, but with the simulated radiances rather than the differences between the experimental and control spectra.

2 Isoprene Regressions

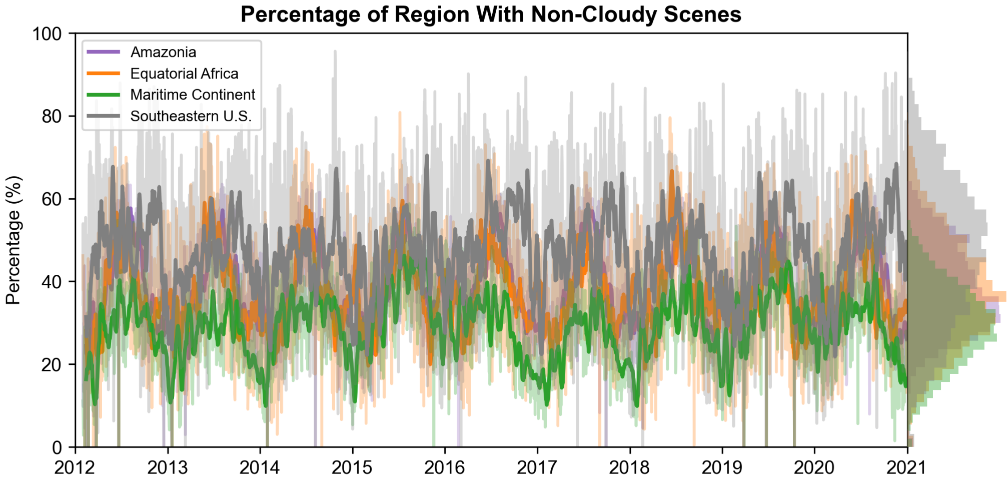

Figure S5: **Data coverage over the three tropical regions.** The percentage of the given region with non-cloudy scenes every day, with the 14-day centered rolling mean overlaid on top. All three tropical regions of interest are plotted, as well as the Southern United States (bounding box: [minimum longitude = -98.525391, minimum latitude = 24.607069, maximum longitude = -68.291016, maximum latitude = 40.446947]) for comparison. On the right are histograms showing the distributions of all four regions.

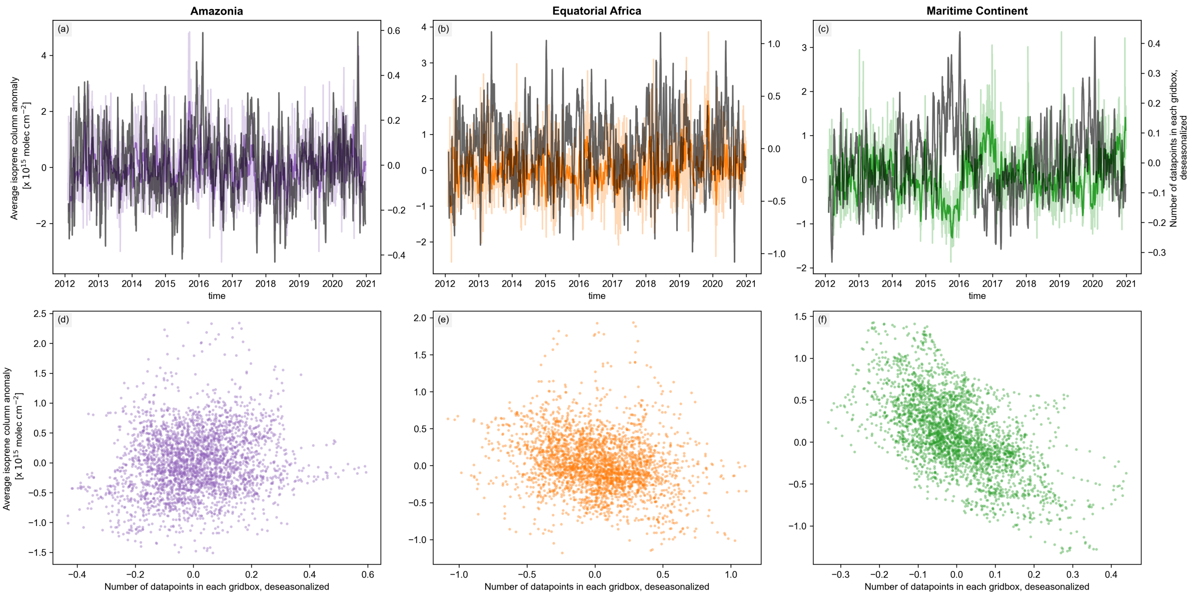

Figure S6: **Data coverage over the three tropical regions.** (a, b, c) The correlation between the average number of non-cloudy CrIS footprints within each 0.5° x 0.625° gridbox (in black, deseasonalized) and the spatially-averaged isoprene column anomaly (in color) for the three tropical regions. Both variables are smoothed using a 14-day centered rolling mean. (d, e, f) The same 14-day centered rolling means plotted against each other.

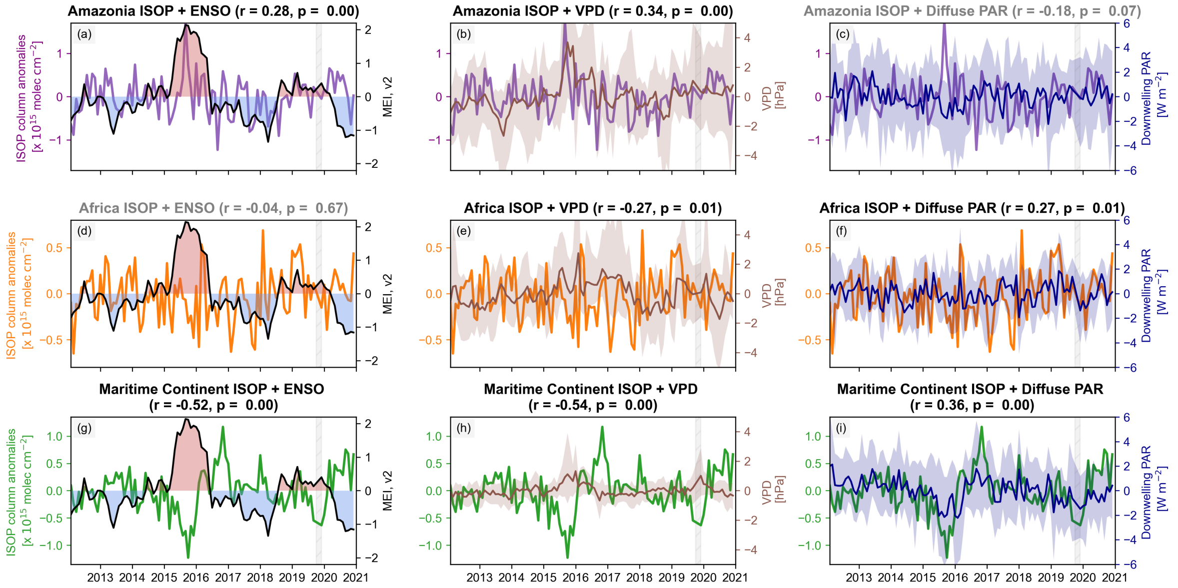

Figure S7: **Additional isoprene regressions.** Figure 2 in the manuscript, but with vapor pressure deficit (VPD) in subplots (b), (e), and (h); and diffuse PAR in subplots (c), (f), and (i). Both quantities were calculated from MERRA-2 reanalysis. All VPD and diffuse PAR correlations are statistically significant ($p < 0.05$) except for Amazonian isoprene and diffuse PAR in subplot (c).

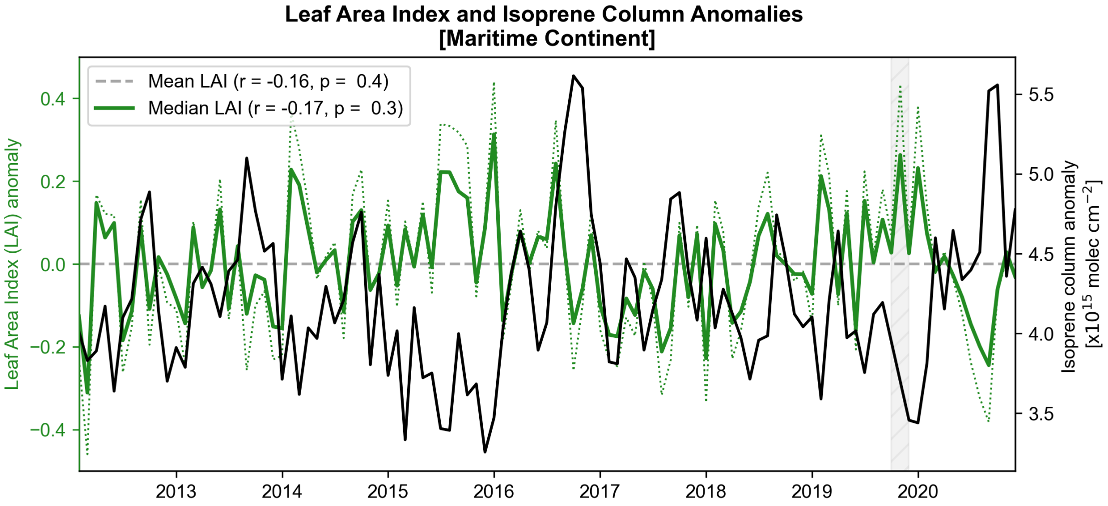

Figure S8: **Leaf area index in the Maritime Continent.** Leaf area index (LAI) spatially-averaged over the Maritime Continent (green), with the anomaly calculated relative to the 2012–2020 LAI mean (solid) or median (dashed). Plotted against LAI is the Maritime Continent isoprene column anomaly (solid black) relative to the 2012–2020 CrIS isoprene column monthly average. LAI observations were obtained from the MODIS MCD15A3H 4–day product and resampled to monthly values.

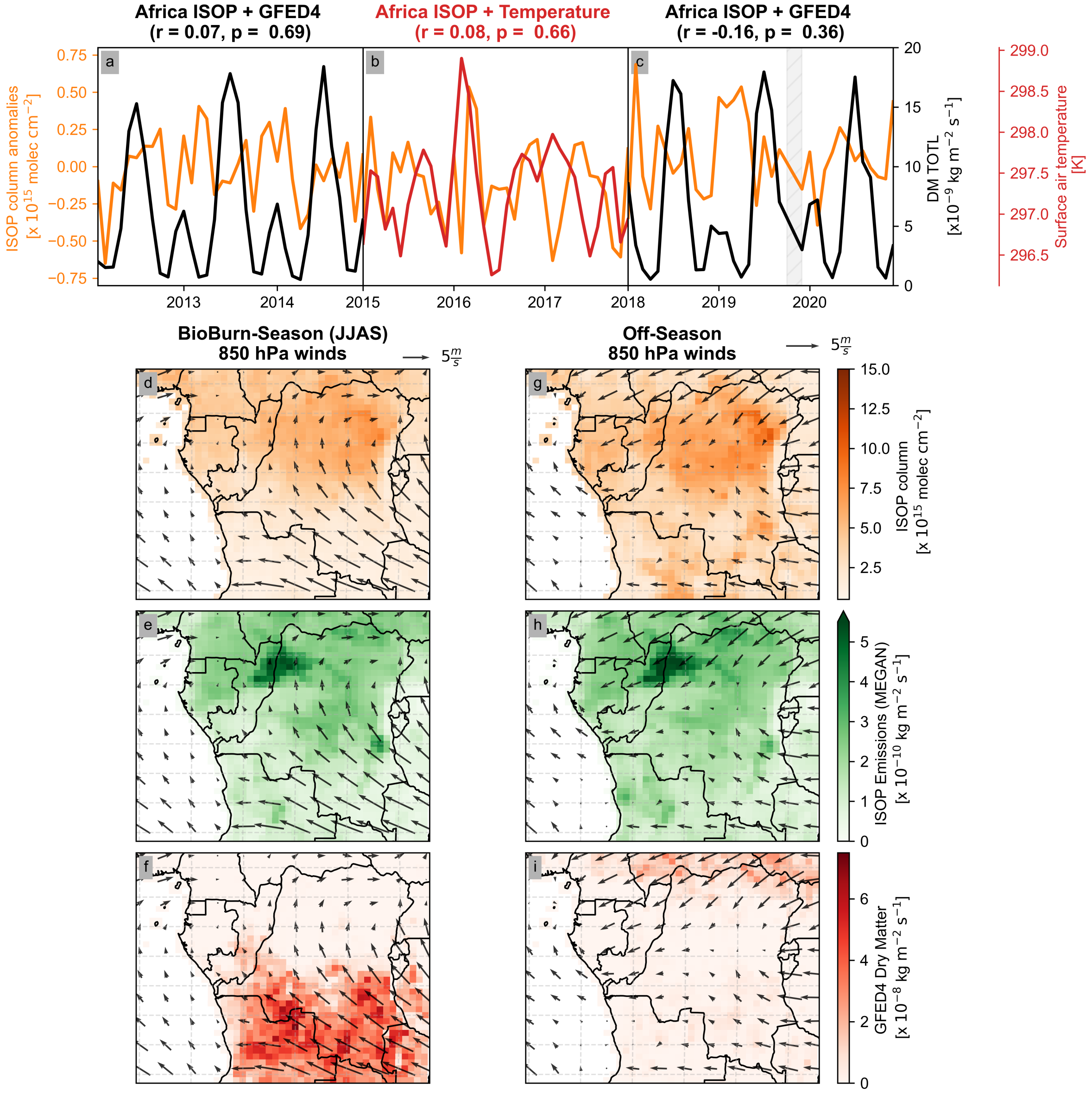

Figure S9: **Non-anomalized values in Africa.** Figure 7 in the manuscript but with GFED4 dry matter and surface air temperature from MERRA-2 plotted in (a, c) and (b), respectively.

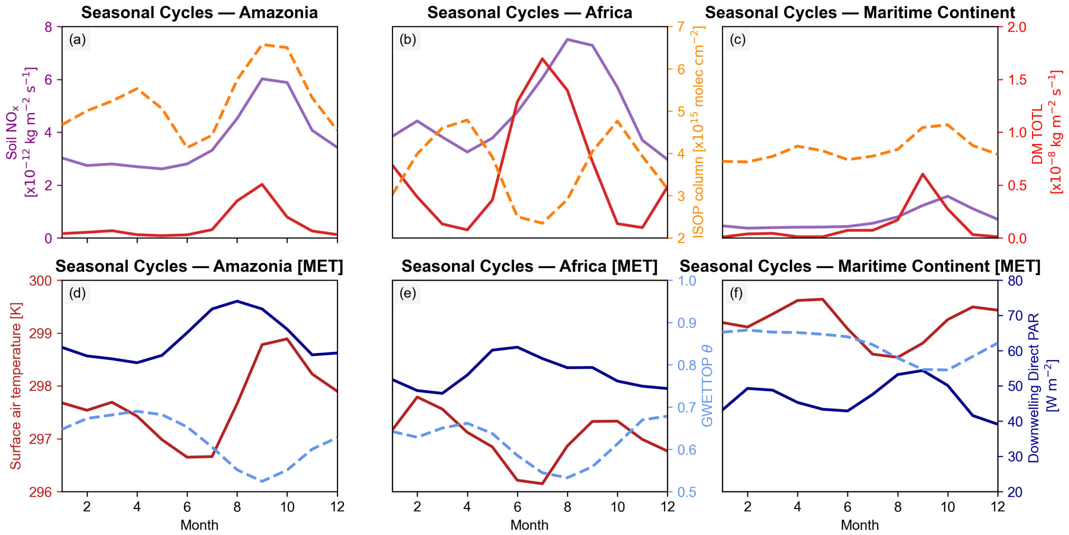

Figure S10: **Seasonal cycles.** Top row (a-c): Seasonal cycles (2012–2020) of soil NO_x (in solid purple, from the offline GEOS-Chem inventory parametrized by BDSNP), GFED4 burned dry matter (solid red), and CrIS isoprene columns (dashed yellow) across the three tropical regions. When spatially-averaged, equatorial Africa has the highest biomass burning and the highest soil NO_x fluxes, while the Amazon has the highest isoprene columns. Bottom row (d-f): Seasonal cycles (2012-2020) of surface air temperature (in red, solid, K), downwelling direct PAR (in dark blue, solid, W m^{-2}), and soil wetness (light blue, dashed), across the three tropical regions. All meteorological variables are taken from MERRA-2 reanalysis.

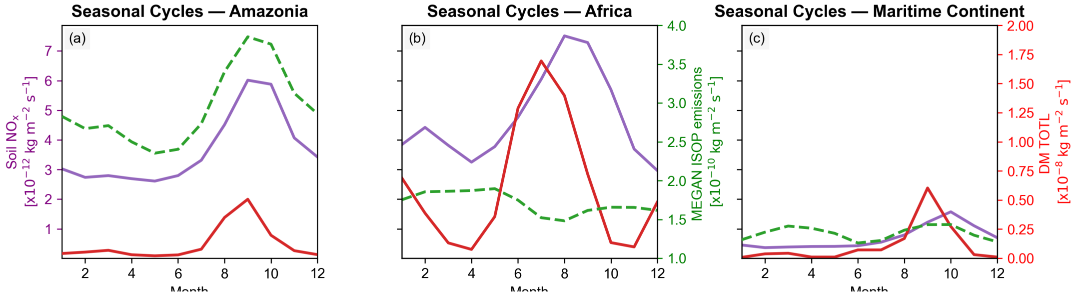

Figure S11: **Seasonal cycles.** Figure S10 but with isoprene emissions from offline MEGAN emissions (dashed green) rather than CrIS isoprene columns. In the Amazon, MEGAN isoprene emissions miss a seasonal April peak, and in the Maritime Continent, isoprene emissions are underpredicted in September/October relative to the CrIS seasonal cycle.

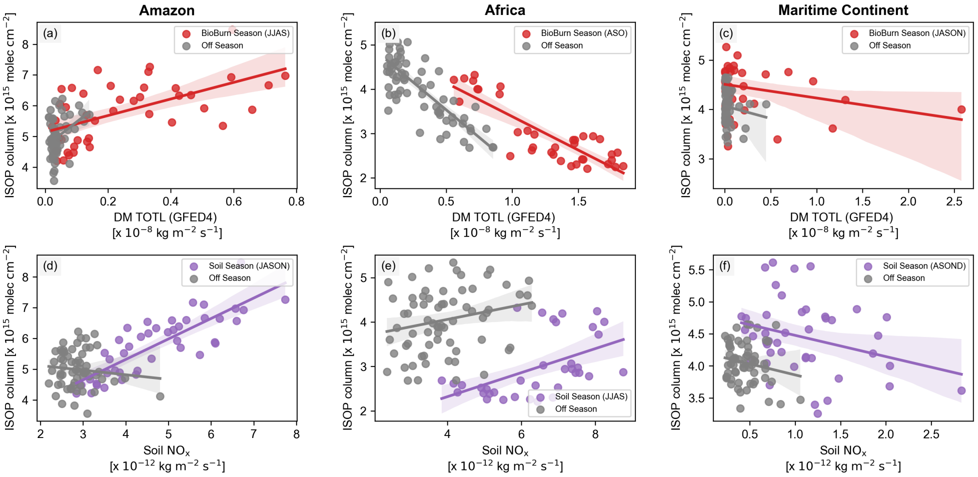

Figure S12: **Seasonal cycles.** CrIS isoprene columns versus biomass burning dry matter (top row) and offline BDSNP soil NO_x (bottom row). Months with the highest biomass burning or soil NO_x emissions are colored in red and purple, respectively, while the rest of the year is in gray. Plotted on top of the data are linear regressions with shaded uncertainties. The strongest negative correlation between NO_x sources and isoprene is in equatorial Africa (biomass burning and isoprene). This correlation may reflect causality (biomass burning NO_x causing changes in isoprene), or it may reflect isoprene emissions and NO_x having opposite seasonal cycles (see Figure S12).

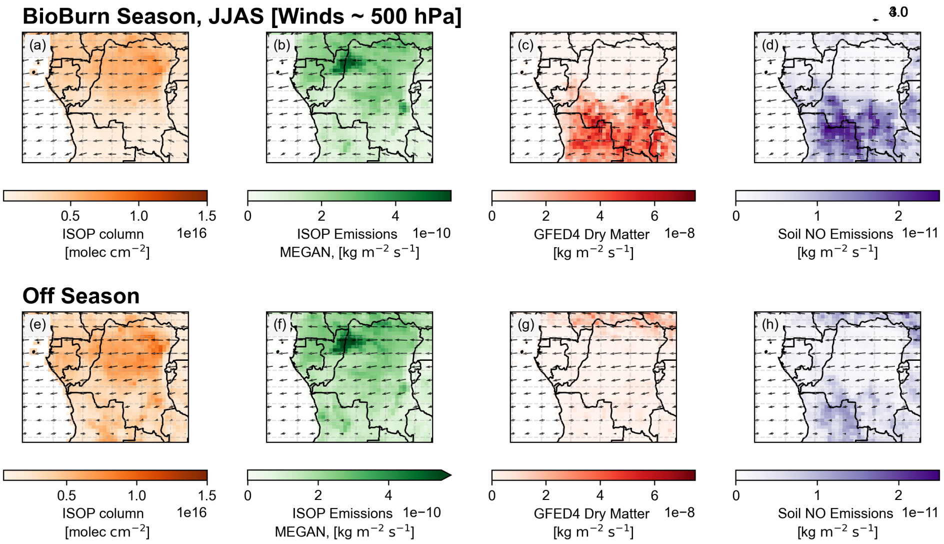

Figure S13: **Spatial heterogeneity in Equatorial Africa.** Same as Figure 7 (subplots d–i) but with winds at GEOS-Chem's vertical box 23 (approximately 500 hPa) instead of box 10 (850 hPa). The winds at 500 hPa are largely easterly with small meridional components.

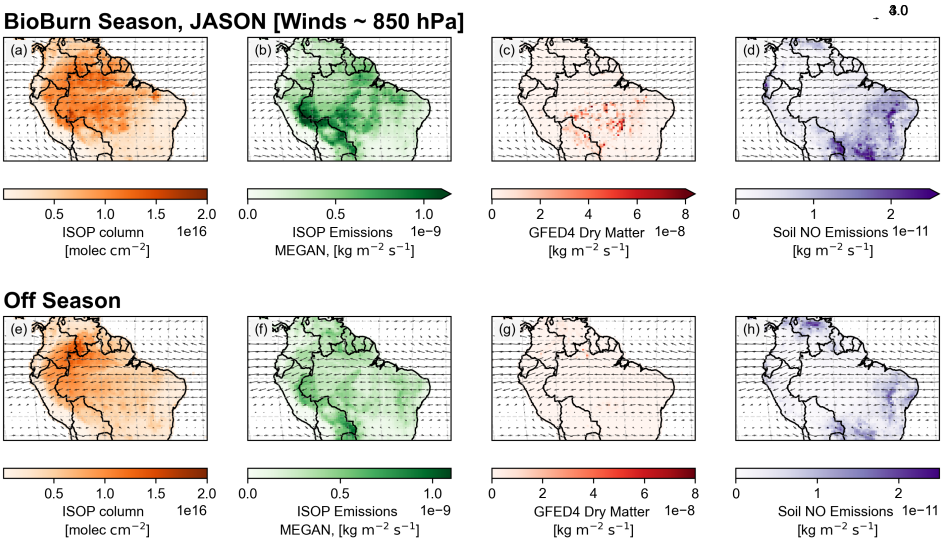

Figure S14: **Spatial heterogeneity in Amazonia.** Similar to Figure S13, but for the Amazon basin and with winds at 850 hPa. The top row shows isoprene columns (a), MEGAN isoprene emissions (b), GFED4 burned dry matter (c), and soil NO_x emissions from BDSNP during the Amazon's biomass burning season (June–November), while the bottom row shows the same quantities but for the rest of the year. Winds at box 10 of the GEOS-Chem vertical grid ($\tilde{8}50$ hPa) from MERRA-2 reanalysis are displayed as vectors.

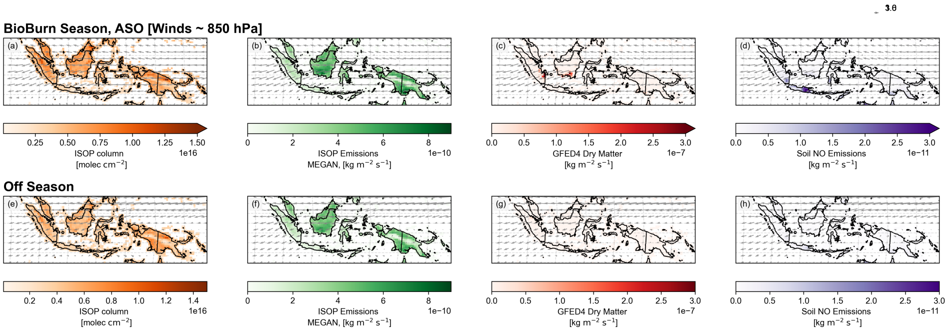

Figure S15: **Spatial heterogeneity in the Maritime Continent.** Similar to Figure S13, but for the Maritime Continent. The top row shows isoprene columns (a), MEGAN isoprene emissions (b), GFED4 burned dry matter (c), and soil NO_x (d) emissions from BDSNP during the Maritime Continent's biomass burning season (August–October), while the bottom row shows the same quantities but for the rest of the year. Winds at box 10 of the GEOS-Chem vertical grid (approximately 850 hPa) are displayed as vectors.

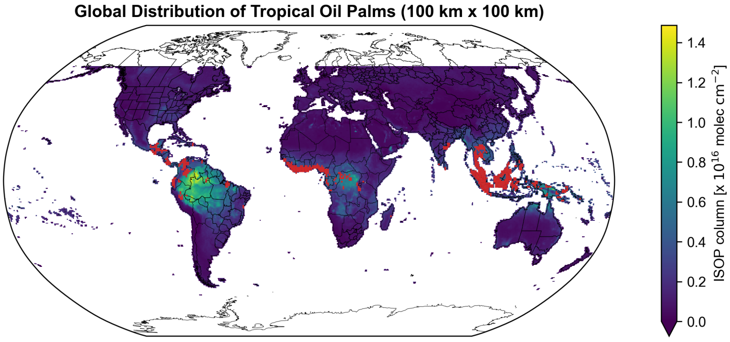

Figure S16: **Global isoprene and oil palm distributions.** Map of CrIS isoprene columns, averaged over 2012–2020, with tropical oil palm detections (100 x 100 km grid boxes) overlaid in red. Grid boxes were obtained from Sentinel-1 and Sentinel-2 images processed by a convolutional neural network from Descals et al. (2021). The Maritime Continent has the highest concentration of oil palm plantations, with oil palms only covering significant areas of west Africa (not included in our equatorial Africa bounding box) and the northwest corner of the Amazon rainforest.

3 GEOS-Chem NO_x Sensitivity Studies

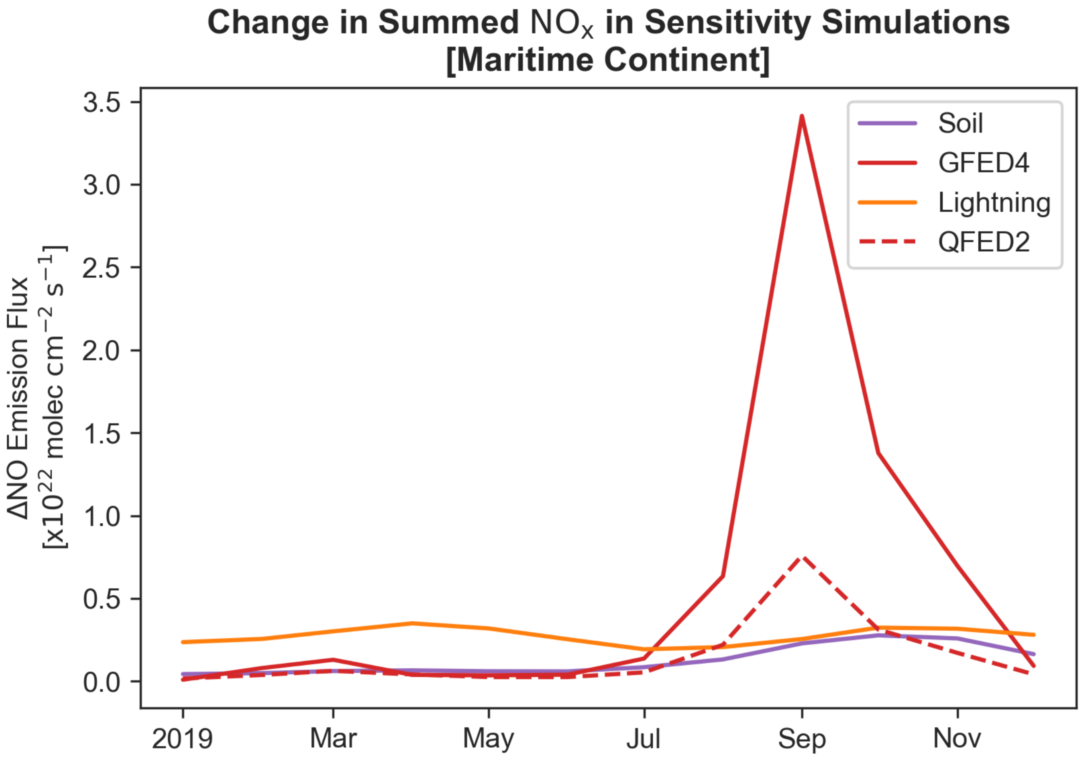

Figure S17: **ΔNO Emission Fluxes.** Changes in NO_x emission fluxes for each run, summed over the GEOS-Chem column. These flux changes correspond to a 10% decrease in NO_x emissions for each of the following sources: GFED4 biomass burning (solid red), offline BDSNP soil NO (purple), lightning NO (orange), and QFED2 biomass burning (dashed red).

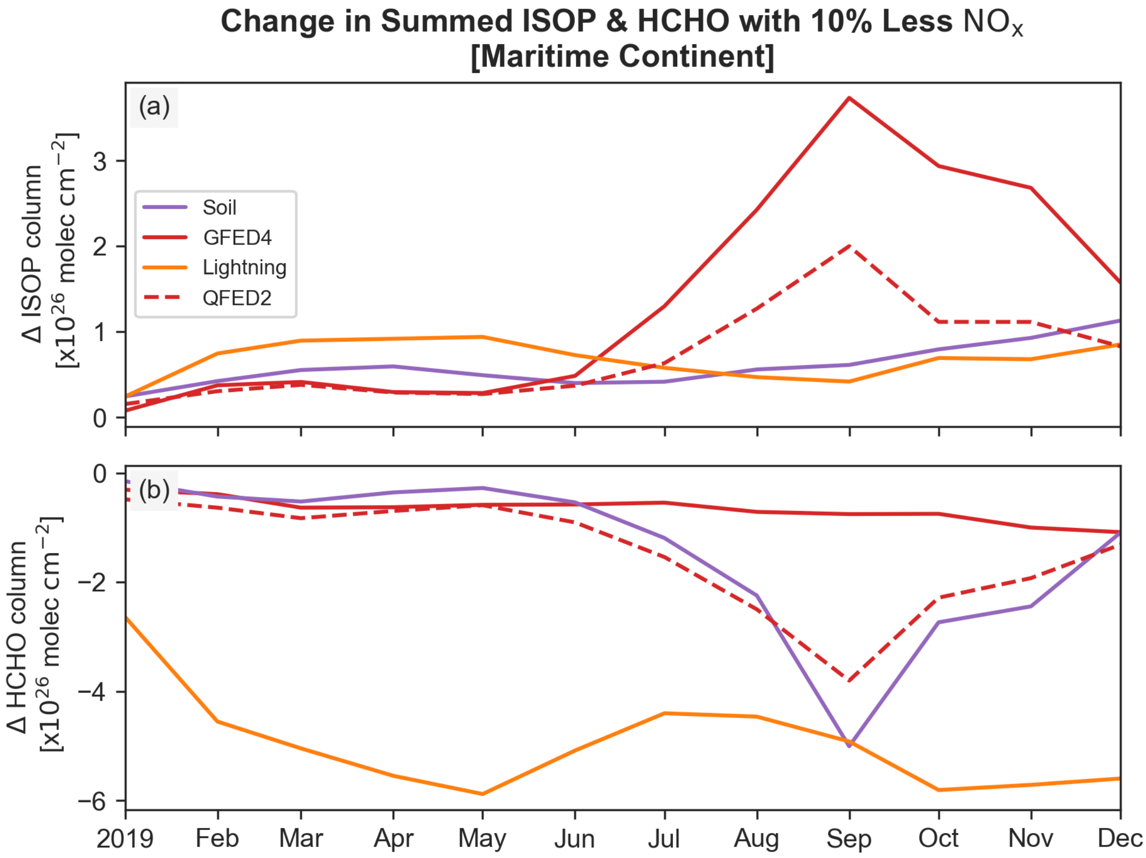

Figure S18: **ΔIsoprene and ΔHCHO in response to ΔNO_x over the Maritime Continent.** (a) The change in isoprene columns, summed over the entire Maritime Continent bounding box, with a 10% decrease in the listed NO_x source. (b) The change in the formaldehyde column for the same NO_x perturbation. In general, a decrease in NO_x decreases formaldehyde but increases isoprene.

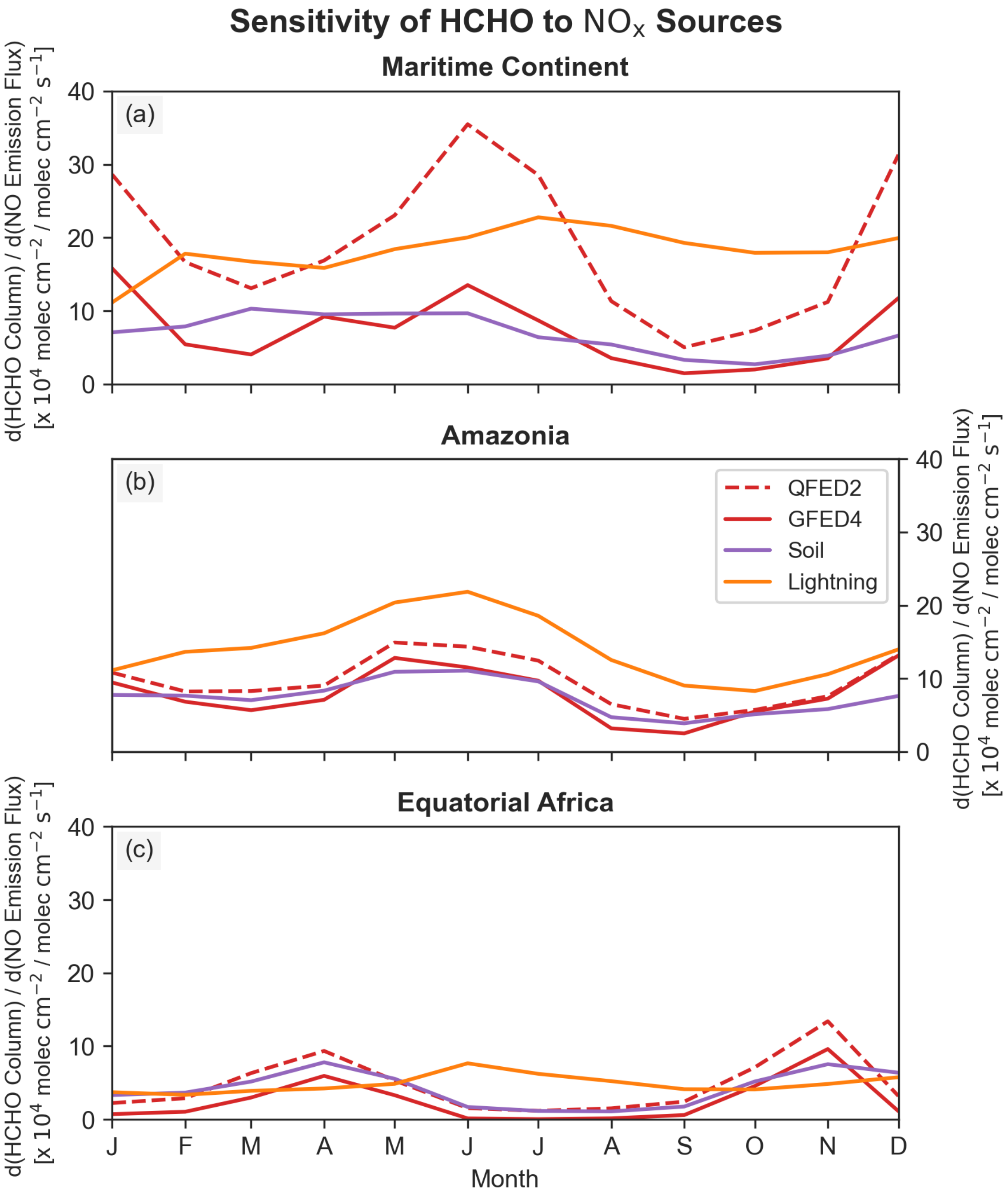

Figure S19: **ΔHCHO in response to ΔNO_x.** Analogous plot to Figure 8 in the manuscript, but depicting the sensitivity of HCHO to perturbations in NO_x sources for the Maritime Continent (a), Amazonia (b), and equatorial Africa (c). In this plot, we show the absolute value, since a decrease in NO_x always decreases formaldehyde. Thus, the direction of the NO_x response is opposite for isoprene and formaldehyde.

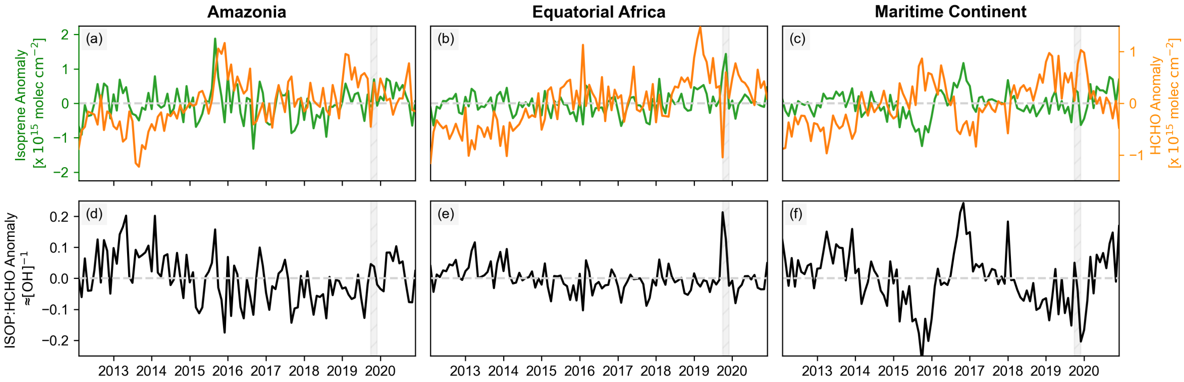

Figure S20: **Implications for the ISOP:HCHO ratio.** Figure 9 in the manuscript, but with the deseasonalized, spatially-averaged ISOP:HCHO over the three regions in the bottom row (d, e, f) for the Amazon, equatorial Africa, and the Maritime Continent, respectively.

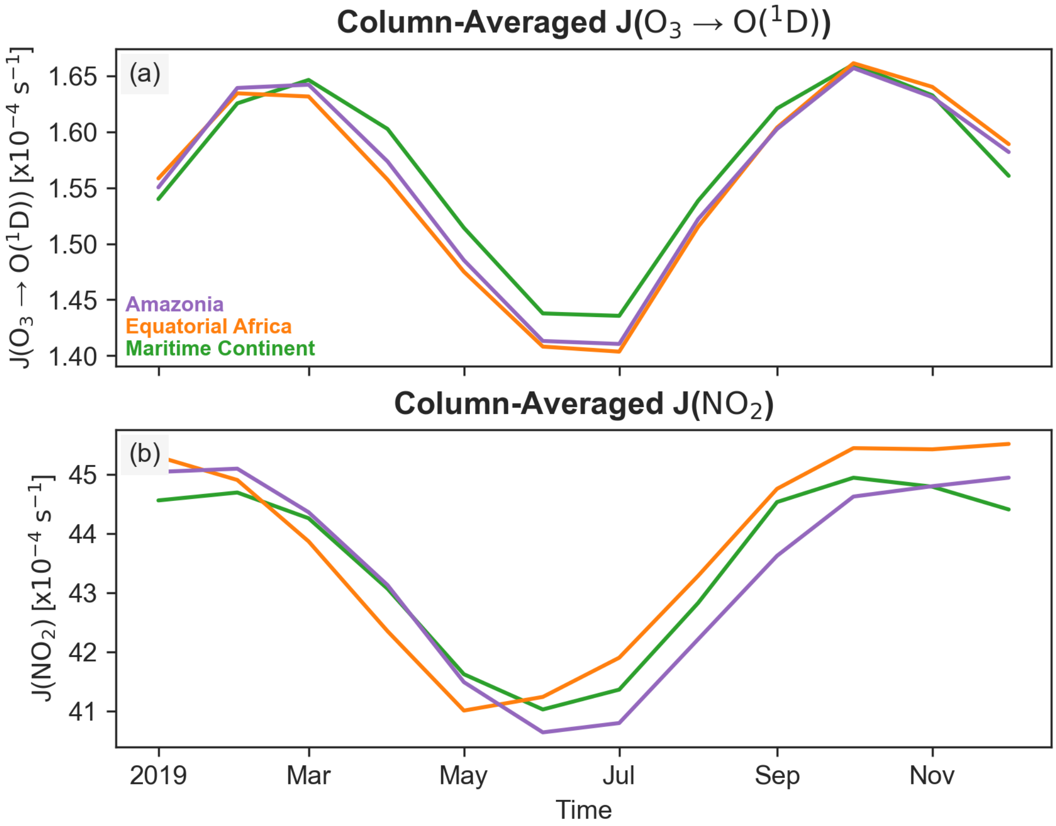

Figure S21: **Differences in photolysis rates.** (a) The column-averaged O_3 photolysis rate over the three tropical regions: Amazonia (purple), equatorial Africa (orange), and the Maritime Continent (green). (b) Same as (a) but with the NO_2 photolysis rate.

References

Brauer, C. S., Blake, T. A., Guenther, A. B., Sharpe, S. W., Sams, R. L., & Johnson, T. J. (2014). Quantitative infrared absorption cross sections of isoprene for atmospheric measurements. *Atmospheric Measurement Techniques*, *7*(11), 3839–3847. https://doi.org/10.5194/amt-7-3839-2014

Descals, A., Wich, S., Meijaard, E., Gaveau, D. L. A., Peedell, S., & Szantoi, Z. (2021). High-resolution global map of smallholder and industrial closed-canopy oil palm plantations. *Earth System Science Data*, *13*(3), 1211–1231. https://doi.org/10.5194/essd-13-1211-2021